

Plasmonic-Enhanced NIR-II Downconversion Fluorescence beyond 1500 nm from Core–Shell–Shell Lanthanide Nanoparticles

Jiamin Xu, Ming Fu, Chengyu Ji, Anthony Centeno, Dong Kuk Kim, Koen Evers, Sandrine E. M. Heutz, Rupert Oulton, Mary P. Ryan, and Fang Xie*

This paper reports on the light amplification of $\text{NaGdF}_4:\text{Yb,Er,Ce}@ \text{NaGdF}_4:\text{Yb,Nd}@ \text{NaGdF}_4$ core–shell–shell downconversion nanoparticles (CSS-DCNPs) in the near-infrared second biological window (NIR-II: 1000–1700 nm) by plasmonic nanostructures. Through a precisely controlled plasmonic metallic nanostructure, fluorescence from Yb^{3+} induced 1000 nm emission, Nd^{3+} induced 1060 nm emission, and Er^{3+} induced 1527 nm emission are enhanced 1.6-fold, 1.7-fold, and 2.2-fold, respectively, under an 808 nm laser excitation for the CSS-DCNPs coupled with a gold hole-cap nanoarray (Au-HCNA), while the Er^{3+} induced 1527 nm emission under a 980 nm laser excitation is enhanced up to 6-fold. To gain insight into the enhancement mechanism, the plasmonic modulation of Er^{3+} induced NIR-II emission at 1550 nm under 980 nm excitation is studied by FDTD simulation and lifetime measurements, showing the observed fluorescence enhancement can be attributed to a combination of enhanced excitation and an increased radiative decay rate.

nanomaterials, such as single-walled carbon nanotubes,^[2] organic molecular dyes,^[3] and inorganic quantum dots,^[4] have been considered. Currently, these materials suffer from broadband emission (>300 nm), photobleaching and toxicity concerns. A promising alternative to overcome these drawbacks are NIR-II emitting lanthanide downconversion nanoparticles (DCNPs).^[5] DCNPs are typically comprised of a low-phonon-energy host matrix (such as NaYF_4 ,^[6] BaLuF_5 ,^[7] NaGdF_4 ^[8]), and a series of suitable lanthanide ions (excluding Y, Lu, Gd) that can be incorporated into the host material. Such a heavy-metal-free ensemble can considerably reduce both ecotoxicological and environmental hazards. The energy band transitions of lanthanide ions are localized within the 4f inner orbitals, shielded by the filled 5s and 5p sub-orbitals. Therefore, the DCNPs

have several spectroscopic merits such as increased fluorescence lifetime, larger Stokes shifts, narrow emission peaks, and they do not show any photoblinking.^[9]

Despite these excellent optical features, low NIR-II downconversion luminescence (DCL) efficiency remains a challenging issue. Due to the partially allowed 4f–4f transitions of lanthanide ions in the host matrix, DCNPs exhibit extremely low absorbance at their narrow absorption bands.^[10] Moreover, the optimum

1. Introduction

Fluorescence biosensing and bioimaging techniques in the near-infrared second biological window (NIR-II: 1000–1700 nm) are at the forefront of research due to the minimal auto-fluorescence and reduced scattering of low energy photons, which enable a higher penetration depth in biological media and a high signal-to-noise ratio.^[1] Recently, a variety of NIR-II luminescent

J. Xu, C. Ji, D. K. Kim, K. Evers, S. E. M. Heutz, M. P. Ryan, F. Xie
Department of Material
Royal School of Mines
Imperial College London
South Kensington Campus, London SW7 2AZ, UK
E-mail: f.xie@imperial.ac.uk

M. Fu, R. Oulton
Department of Physics
Blackett Laboratory
Imperial College London
South Kensington Campus, London SW7 2AZ, UK
A. Centeno
James Watt School of Engineering
University of Glasgow
Glasgow G12 8QQ, UK

The ORCID identification number(s) for the author(s) of this article can be found under <https://doi.org/10.1002/adom.202300477>

© 2023 The Authors. Advanced Optical Materials published by Wiley-VCH GmbH. This is an open access article under the terms of the Creative Commons Attribution License, which permits use, distribution and reproduction in any medium, provided the original work is properly cited.

DOI: 10.1002/adom.202300477

luminescence intensity of lanthanide nanoparticles is observed at a relatively low dopant concentration. The exact reason for this limitation is still under debate.^[11] One possible explanation is that the highly doped ions would lead to detrimental interactions, such as the energy cross-relaxation between the adjacent dopants and the consecutive long-distance energy migration from emitting centers to surface defects, which jointly result in the depopulation of excited states and quenching effects.^[12]

Researchers have reported several strategies to improve the emission efficiency of lanthanide nanoparticles, including cation incorporation, core-shell structure design, and plasmonic modulations. For example, Zhong et al. reported that an addition of 2% Ce³⁺ ions into NaYF₄:Er nanocrystals could generate a 9-fold NIR-II DCL enhancement with a bright 1550 nm emission under 980 nm excitation.^[13] Later, Li et al. reported the NIR-II DCL at 1525 nm under an 808 nm excitation was considerably boosted by introducing 2% Ce into the Nd-sensitized NaYF₄:Gd,Yb,Er,Nd core nanoparticles. With growing a layer of Nd doped NaYF₄ shell, the NIR-II DCL intensity was improved by 11 times, compared to Ce³⁺ free core nanoparticles.^[14] Recently, Li et al. reported NIR-II emission enhancement from Li⁺ and Zr⁴⁺ doped NaGdF₄:Yb,Er Nanocrystals.^[15]

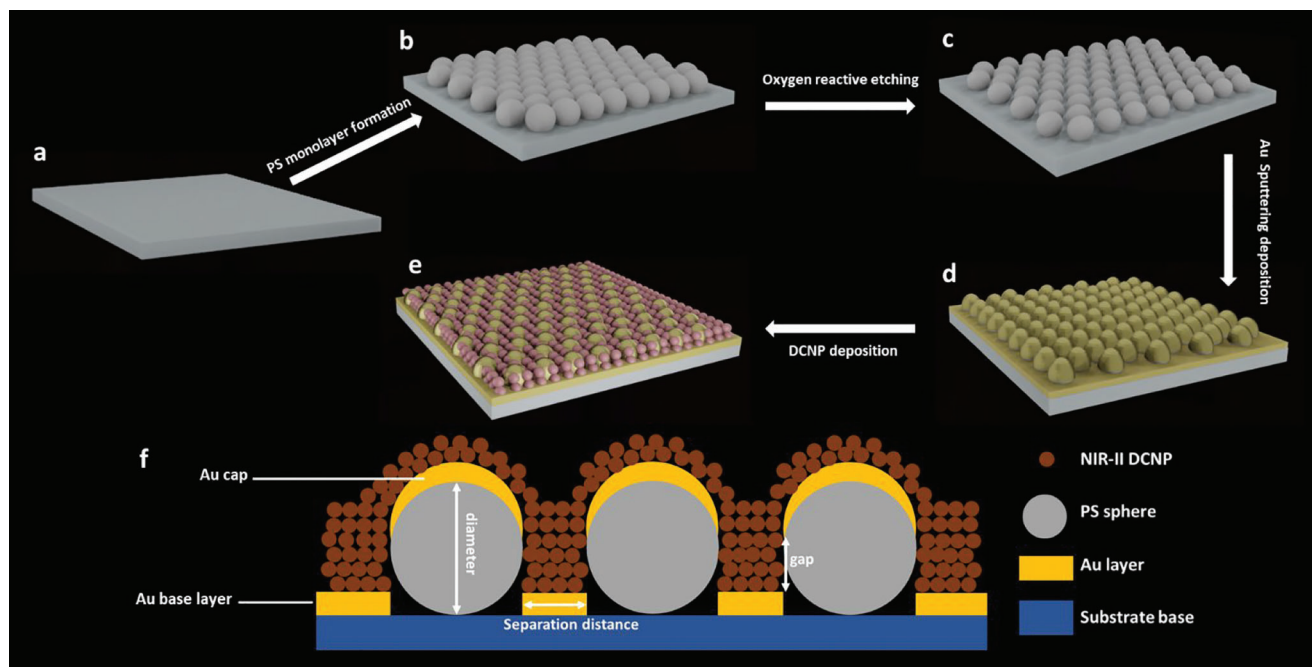
By using metallic nanostructures as optical antennas, it is possible to generate large localized electric field “hot spots” in the proximity of the metallic surface due to surface plasmon resonance (SPR). The emission intensity of fluorophores in the vicinity of those “hot spots” can be enhanced by orders of magnitude under illumination at the SPR frequency of the nanostructure.^[16] There have been both theoretical and experimental studies on using plasmonic modulation to amplify the visible upconversion luminescence (UCL) from lanthanide nanoparticles, primarily aimed at solar energy harvesting.^[17] Various types of plasmonic substrates have been purposefully designed to pursue a higher UCL enhancement factor, including Ag nanograting film,^[18] Au nanohole arrays,^[19] vertically aligned gold nanorod substrate,^[20] etc.

To the best of our knowledge, this work is the first to report plasmonic modulation of NIR light-responsive lanthanide nanoparticles showing NIR-II DCL emission enhancement. For applications of fluorescence in biomedical fields, enhancing both the excitation and emission bands within the biological transparency windows are very attractive. Therefore, we consider the plasmonic enhancement of NIR-II DCL from NaGdF₄:20%Yb,2%Er,4%Ce@NaGdF₄:10%Yb,5%Nd@NaGdF₄ core-shell-shell (CSS) DCNPs coupled with an Au hole-cap nanoarray (Au-HCNA) excited at wavelengths of 808 and 980 nm, respectively. The first biological window encompasses both 808 and 980 nm lasers, providing a significant advantage in achieving a high level of light transmission through biological tissue while minimizing damage to surrounding tissues. Additionally, using an 808 nm laser for excitation can optimize excitation efficiency and prevent over-heating effects, making it a favorable option over the 980 nm wavelength. With a simple and robust colloidal lithography technique, two types of Au-HCNAs were fabricated using different reactive ion etching (RIE) times (labelled as “Au50-HCNA” and “Au60-HCNA” substrates), showing distinctive spectroscopic characteristics. To minimize surface contact quenching, the separation distance between DCNPs and Au-HCNA was controlled by growing

successive shells over the core nanoparticles. As a result, when the CSS-DCNP hybridized Au-HCNA films were excited under 808 nm irradiation, emission intensity from Er³⁺ induced UCL at 540 nm was enhanced up to 7.6-fold, whilst the intensity of Er³⁺ induced 1527 nm emission was enhanced by 2.2-fold. In addition, we observed that the NIR-II DCL emissions of Yb³⁺ induced 1000 nm and Nd³⁺ induced 1060 nm emission were enhanced by ≈1.6-fold and 1.7-fold, respectively. When a 980 nm laser was used, an up to 6.5-fold enhancement of Er³⁺ induced 1527 nm emission was obtained. FDTD simulations showed that the highest local field intensities of Au-HCNA under both 808 nm and 980 nm excitations were located between adjacent Au caps (**Scheme 1**). Fluorescence lifetime measurements using a 980 nm excitation showed a dramatic decrease in Er³⁺ induced 1550 nm emission lifetime when CSS-DCNPs were coupled with a Au50-HCNA film. These results indicate that a combination of excitation enhancement and an increased radiative decay rate contribute to the observed fluorescence enhancement. The feasibility of modulating surface plasmon resonance to improve NIR-II DCL emission from DCNPs is demonstrated in this work. This is significant for the future design of an efficient NIR-II luminescent platform for the biosensing and bioimaging applications.

2. Results and Discussion

The multilayer DCNPs incorporated with a series of lanthanide ions into the core and shell layers were synthesized through a co-precipitation method. As is shown from TEM images (**Figure 1a–c**) and the corresponding EDX spectra (**Figure S1a–c**, Supporting Information), the core nanoparticle was tri-doped with Yb³⁺, Er³⁺, Ce³⁺ ions and showed a uniform size distribution of $\approx 7.1 \pm 1.0$ nm in diameter. Subsequently, a thin shell of $\approx 3.4 \pm 0.9$ nm containing Yb³⁺ and Nd³⁺ ions was grown onto the core nanoparticle, with an observation of the increased nanoparticle size ($\approx 14.9 \pm 1.3$). Finally, an inert shell was coated over the core-shell (CS) nanoparticles, and the overall shell thickness reached $\approx 5.9 \pm 1.6$ nm. All the synthesized nanoparticles showed excellent dispersibility in the nonpolar cyclohexane solvent and formed a stable yellow transparent solution (**Figure S1a**, Supporting Information), which was ascribed to the protection of long-chain oleic acid as the capping ligands. The elemental mapping of the single core/shell/shell (CSS) nanoparticle (**Figure 1g**) confirmed the major compositions were Na, Gd, F, and Yb, while the presence of trace amounts of Ce, Er and Nd ions were proved from EDX spectra of core and CS DCNPs, respectively (**Figure S1b,c**, Supporting Information). XRD patterns (**Figure 1i**) revealed the diffraction peaks of the core, CS and CSS DCNPs could be indexed to the standard card of NaGdF₄ (JCPDS No. 00-027-0699) with a typical hexagonal crystalline structure. This was in good agreement with the measurements from the lattice fringes (**Figure 1c**, inset) and diffraction ring pattern (**Figure 1h**). For this designed DCNP, the hexagonal NaGdF₄ was selected as the host material due to its superior nature of low photon energies and high chemical stability. The incorporated Er³⁺, Yb³⁺, and Nd³⁺ were different types of emitting ions, namely, activators. Nd³⁺ dually acted as the “sensitizer” to harvest NIR irradiation, whilst Yb³⁺ dually acted as the “bridge” to modulate energy migration from sensitizer to activator.



Scheme 1. Schematic illustration of the workflow of MEF on Au-HCNA films: a) The pristine FTO glass slide, b) Formation of a PS self-assembled film, c) Self-assembled shrunk PS film through RIE, d) Deposition of Au film through PVD, e) Deposition of DCNPs through drop-casting. f) Cross-sectional illustration of DCNP/Au-HCNA hybrid film for the enhanced NIR-II fluorescence emission.

The fluorescence spectra in **Figure 2a,b** show the multiband emission features of CSS-DCNPs ranging from visible to NIR-II regions under 808 nm and 980 nm excitation, respectively, implying a cascade of radiative and nonradiative decay processes that may occur within the DCNPs. **Figure 2c** shows evidence that the incorporated Nd^{3+} could efficiently harvest an 808 nm light source, compared to Yb^{3+} which can only harvest lower energy light at 980 nm. **Figure 2d** illustrates the luminescence pathways of the designed CSS-DCNPs. When the nanoparticles were excited by an 808 nm laser, the populated electrons on the $^4\text{F}_{5/2}$ state (Nd^{3+}) hopped onto the adjacent $^2\text{F}_{5/2}$ states (Yb^{3+}) through a phonon-assisted energy transfer process. Simultaneously, a proportion of $^4\text{F}_{5/2}$ state electrons (Nd^{3+}) decayed to the $^4\text{I}_{13/2}$ and $^4\text{I}_{11/2}$ states and emitted NIR-II photons at ≈ 1340 and ≈ 1060 nm, respectively. Regarding the populated electrons on the $^2\text{F}_{5/2}$ (Yb^{3+}) states, the $^2\text{F}_{5/2} \rightarrow ^2\text{F}_{7/2}$ transition led to the DCL emission at ≈ 1000 nm, meanwhile, a proportion of electrons hopped to the $^4\text{I}_{11/2}$ states (Er^{3+}) after frequent energy transfer processes between $\text{Yb}^{3+}\text{-Yb}^{3+}$ and $\text{Yb}^{3+}\text{-Er}^{3+}$. The rich energy-level structure of Er^{3+} allows the electrons on the long-lived mediated $^4\text{I}_{11/2}$ (Er^{3+}) states to be populated into the higher energy levels, which results in the UCL emission at ≈ 522 nm, ≈ 540 nm, and ≈ 660 nm via the radiative $^2\text{H}_{11/2}\text{-}^4\text{I}_{15/2}$, $^4\text{S}_{3/2}\text{-}^4\text{I}_{15/2}$, and $^4\text{F}_{9/2}\text{-}^4\text{I}_{15/2}$ transitions, respectively. The $^4\text{I}_{11/2}$ (Er^{3+}) state electrons can also relax nonradiatively to the $^4\text{I}_{13/2}$ (Er^{3+}) states, then emitting NIR-II photons at ≈ 1527 nm via the $^4\text{I}_{13/2}\text{-}^4\text{I}_{15/2}$ transition. The luminescence pathways and the related energy transfer processes under 980 nm excitation was similar to that under 808 nm excitation, except that Yb^{3+} can directly absorb 980 nm photons and transfer energy to Er^{3+} . Therefore, Nd^{3+} emitted peaks at 1000, 1060, and 1340 nm were nonexistent as shown in **Figure 2b**.

The presence of Ce^{3+} in the same layer of Er^{3+} can increase the $^4\text{I}_{13/2}(\text{Er}^{3+}) \rightarrow ^4\text{I}_{15/2}(\text{Er}^{3+})$ relaxation rate through an energy crossover with $^2\text{F}_{5/2}(\text{Ce}^{3+}) \rightarrow ^2\text{F}_{7/2}(\text{Ce}^{3+})$. To achieve the best NIR-II fluorescence performance peaking at 1527 nm, the concentration of Ce^{3+} was optimized. The optimal concentration of Ce^{3+} in our study was 4% (**Figure S2**, Supporting Information) while further increasing the concentration conversely quenched the fluorescence. This observation was in agreement with previous reports.^[14]

The workflow to fabricate Au-HCNA films via colloidal lithography is shown in **Scheme 1**. The commercial PS spheres were self-assembled to form a well-organized closely packed hexagonal monolayer film on FTO glass substrate. The PS spheres on the substrate were then shrunk by O_2 reactive ion etching (RIE), followed by depositing Au layer with a thickness of 60 nm, which was monitored by a quartz crystal monitor (QCM) in the sputtering system. Finally, DCNPs were deposited via drop-casting to form the DCNPs/Au-HCNA hybrid films. With adjustable diameters of shrunk PS spheres by using different O_2 etching times, Au-HCNAs with variable structural parameters can be made. The morphologies of Au50-HCNA and Au60-HCNA films are visualized by SEM images (**Figure 2a,b**), and their corresponding structural parameters are summarized in **Table S1** (Supporting Information). The morphologies of two types of Au-HCNA after coating with CSS-DCNPs are shown in **Figure 3d,e**. It was seen that the protruding Au caps of Au-HCNA were immersed by a thick solid layer consisting of DCNPs. Besides, the periodicity of each type of hybrid film was negligibly changed compared to the pristine Au-HCNA. EDX (**Figure S3a**, Supporting Information) indicated the major elements across the surface of the DCNP/Au-HCNA hybrid film contained Au, Na, Gd, F and

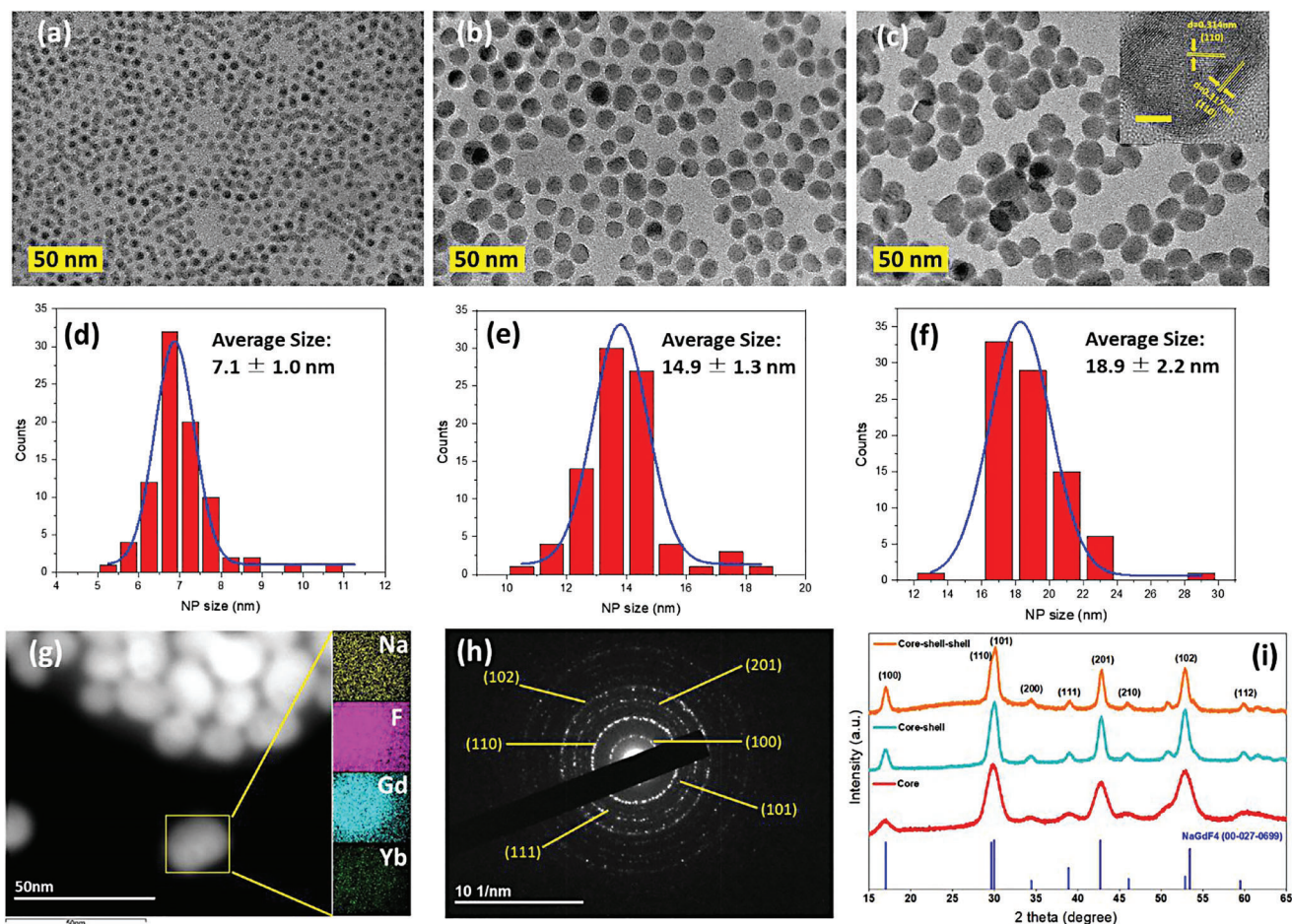


Figure 1. a–c) TEM images of cyclohexane dispersed NaGdF₄: 20%Yb/4%Ce/2%Er core, NaGdF₄: 20%Yb/4%Ce/2%Er@ NaGdF₄: 10%Yb/5%Nd core/shell (CS), and NaGdF₄: 20%Yb/4%Ce/2%Er@ NaGdF₄: 10%Yb/5%Nd@NaGdF₄ core/shell/shell (CSS) DCNPs, respectively. Inset shows HR-TEM image of single CSS DCNP and inset scale bar is 5 nm. d–f) size distribution histogram of core, CS and CSS DCNPs, respectively. g, h) STEM+EDX and SAED images of CSS DCNPs. i) XRD patterns of as-prepared core, CS, and CSS DCNPs.

Yb, which confirmed a uniform distribution of DCNPs. Topographies of Au50-HCNA film before and after coating with DCNPs were also characterized by AFM (Figure 3e,f). The 3D-depth profiles show the DCNP/Au-HCNA hybrid film was plainer than the pristine Au-HCNA, from which we deduced that DCNPs had entered the trenches between adjacent Au caps and tended to make the surface level. This assumption was supported by the cross-sectional view of DCNP/Au-HCNA hybrid film (Figure S3b, Supporting Information), showing the nanoparticle coating layer was $\approx 108 \pm 10$ nm in thickness, whilst DCNPs were accumulated at the trenches more than on top of Au caps. Based on an average CSS DCNP size of ≈ 19 nm, the observed average thickness of ≈ 108 nm suggests the presence of 5–6 layers of DCNPs.

Extinction spectra of both Au50-HCNA and Au60-HCNA before and after coating with DCNPs were measured and are shown in Figure 3g. For both types of pristine Au-HCNAs, multiple extinction peaks were visualized across the visible and NIR regions. The most intensive peaks at ≈ 900 and ≈ 1000 nm for Au60-HCNA and Au50-HCNA respectively, overlapped with the absorption bands of Nd³⁺ and Yb³⁺. The other two broad peaks around ≈ 550 and ≈ 1600 nm well matched the UCL and DCL emission spec-

tra of Er³⁺. CSS-DCNPs/Au-HCNA hybrid films, for both types, showed a slight blue-shift at their corresponding most-intensive peaks, and showed a slight redshift at the other two broad peaks. There was no evidence that the deposition of DCNPs led to a degradation of the nanostructured film (Figure S4, Supporting Information). Therefore, we assumed that the peak shifts were mainly attributed to the changes in the dielectric environment.

Previous studies have shown the necessity of a separation layer (usually >4 nm) between the metallic surface and fluorophores to prevent surface contact quenching.^[21] For the substrate-based MEF platform, the separation was often achieved by depositing a dielectric or polymeric film of 6–8 nm in thickness such as MoO₃,^[20] SiO₂,^[22] PAH-PSS hybrid electrolytes.^[23] In our study, the separation distance was controlled by directly growing a shell of the same host matrix over the core nanoparticles. For the CS structure, the separation distance between emitter Er³⁺ and Au surface was around ≈ 3.4 nm, while this distance was enlarged to around ≈ 5.9 nm for the CSS structure.

From Er³⁺ induced fluorescence spectra shown in Figures 4a,b, both CS and CSS DCNPs via coupling to the Au50-HCNA, showed enhanced visible UCL and NIR-II DCL emission,

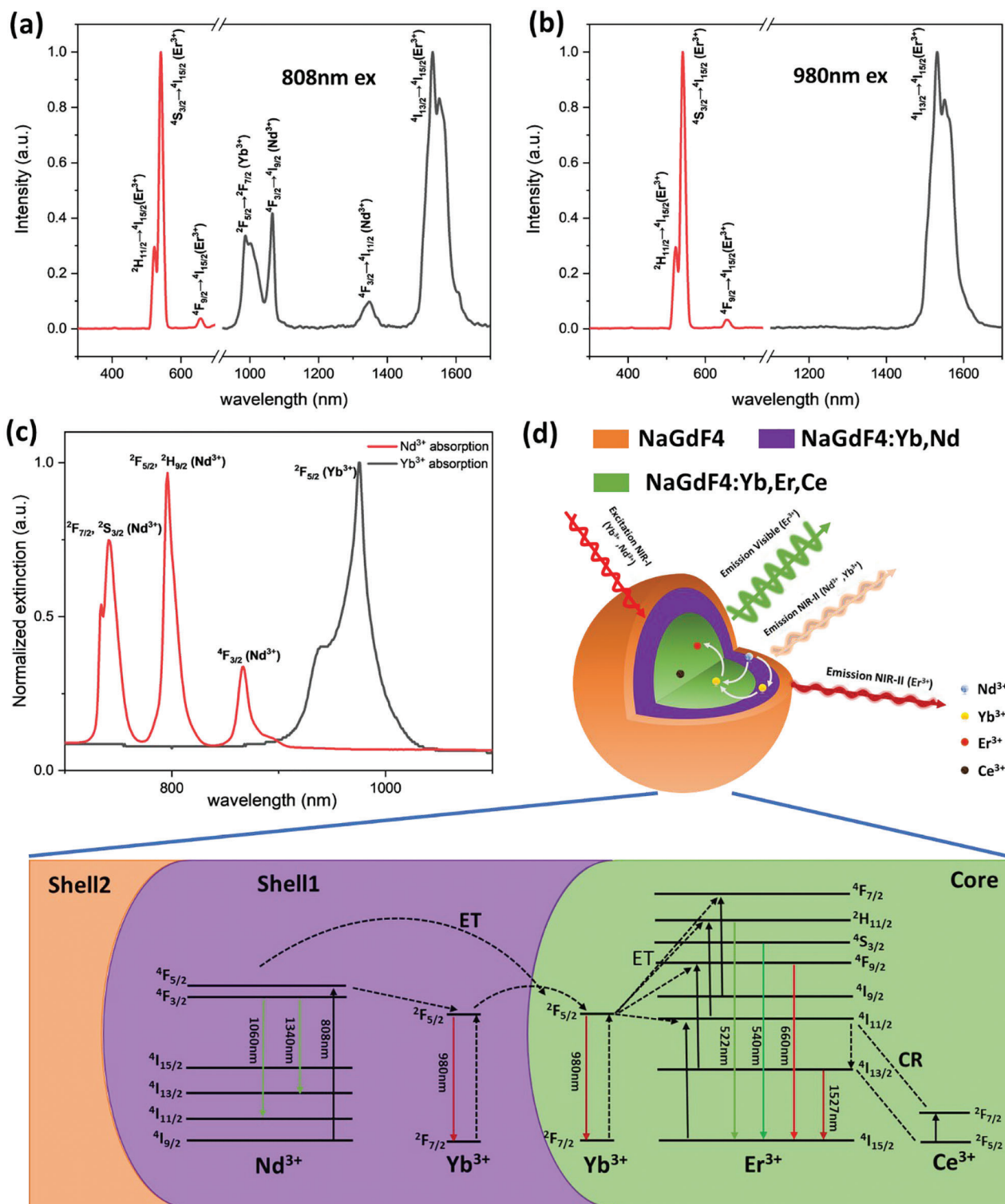


Figure 2. a,b) Fluorescence spectra of CSS-DCNP solution under the c) 808 nm excitation and d) 980 nm excitation. c) Absorption spectra of Nd^{3+} and Yb^{3+} dissolved in aqueous solution d) Schematic illustration of fluorescence emissions and the underlying energy transfer mechanisms of CSS downconversion nanoparticles (CSS-DCNP) under NIR laser excitation.

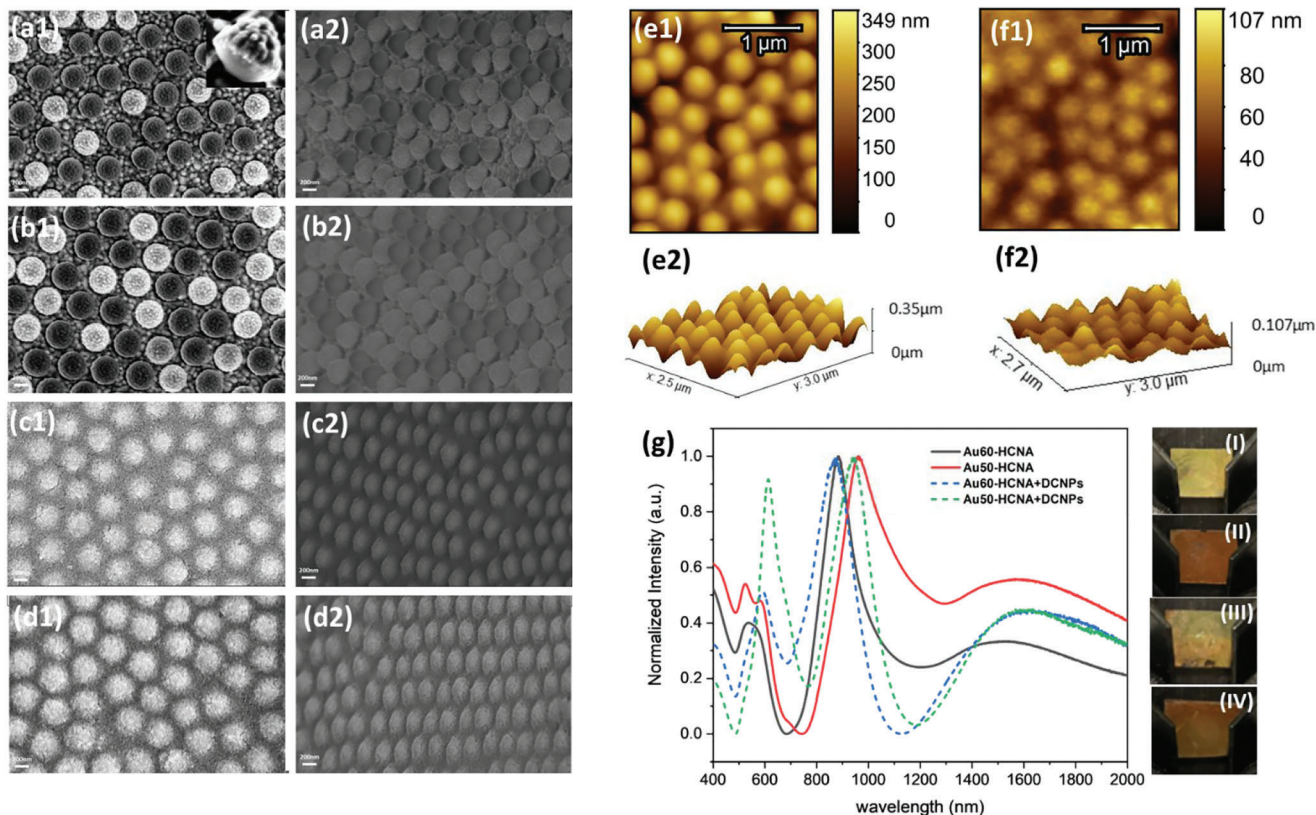


Figure 3. a–d) SEM images of Au60-HCNA, Au50-HCNA, CSS-DCNPs/Au60-HCNA hybrid film and CSS-DCNPs/Au50-HCNA hybrid film, respectively. Scale bar is 200 nm for all images. a1–d1) show the vertical view and a2–d2) show the 60° tilted view of each sample. a1 inset shows the cross-sectional view of single Au cap. e, f) AFM tapping mode images and the corresponding 3D surface visualizations of e1, e2) Au50-HCNA film and f1, f2) CSS-DCNPs/Au50-HCNA hybrid film. g) Extinction spectra of two types of Au-HCNA films before and after depositing DCNPs. Insets (I–IV) show the digital camera images of Au50-HCNA film, Au60-HCNA film, CSS-DCNPs/Au50-HCNA hybrid film and CSS-DCNPs/Au60-HCNA hybrid film, respectively.

compared to their counterparts on pristine FTO glasses (labelled as “reference”). The originally higher fluorescence intensity from CSS nanoparticles compared to CS nanoparticles was attributed to the additional inert shell over CSS nanoparticles, which effectively prevented the quenching induced by surface defects. It was noted that both UCL and DCL emissions were improved more effectively for CS-DCNPs than CSS-DCNPs (Figure 4d), even though the separation distance (SD) from the metal surface to the emitting centers of CS-DCNPs was smaller than 5 nm. One possible reason is that the MEF performed more effectively on those fluorophores with lower quantum yields.^[24] In such a situation, the net fluorescence enhancement via plasmonic modulation on the low-efficient CS-DCNPs could be dominant over emission quenching.

As shown in Figure 4c, NIR-II-DCL emission from Yb³⁺ and Nd³⁺ via coupling to Au50-HCNA could also be improved, although the enhancement was no more than 2-fold. Different from Er³⁺ which was entirely doped inside the core, Nd³⁺ and a portion of Yb³⁺ were doped within the middle shell. Consequently, the separation distance from these emitting ions to the metal surface became variable, depending on their relative positions to the core nanoparticle (Figure 4c, inset). It was worth noting that for the CS configuration, a small part of the shell had direct contact with the metal surface. While for the

CSS configuration, the smallest separation from middle shell to metal was less than 3.4 nm. Hence, the observed emission enhancement factors from Nd³⁺ and Yb³⁺ were probably underestimated.

In general, two categories of plasmonic enhancement modes namely excitation enhancement and emission enhancement were considered when lanthanide luminescent nanoparticles were placed in the vicinity of a metallic nanostructure. Excitation enhancement is caused when the SPR of the metallic nanostructure overlaps the excitation band of the nanoparticles. The excitation of the SPR leads to enhanced localized electric fields. For emission enhancement, the radiative decay rate of SPR coupled fluorophores can be improved by the Purcell effect on the premise that the SPR overlaps the emission band.^[25] Figure 4d shows that the emission intensities of Er³⁺ induced Visible-UCL and NIR-II DCL were increased by up to 7.6-fold and 2.2-fold respectively by the CSS-DCNPs/Au50-HCNA hybrid film, compared to an enhancement of 6.7-fold and 1.9-fold respectively by the CSS-DCNPs/Au60-HCNA hybrid film. For Yb³⁺ and Nd³⁺ induced NIR-II DCL, the enhancement factors from CSS-DCNPs/Au50-HCNA and CSS-DCNPs/Au60-HCNA hybrid films were nearly the same (< 2-fold).

Figure 5 shows the simulated local electric field (E-field) intensity mapping of the two used types of Au-HCNAs at 808 nm. It

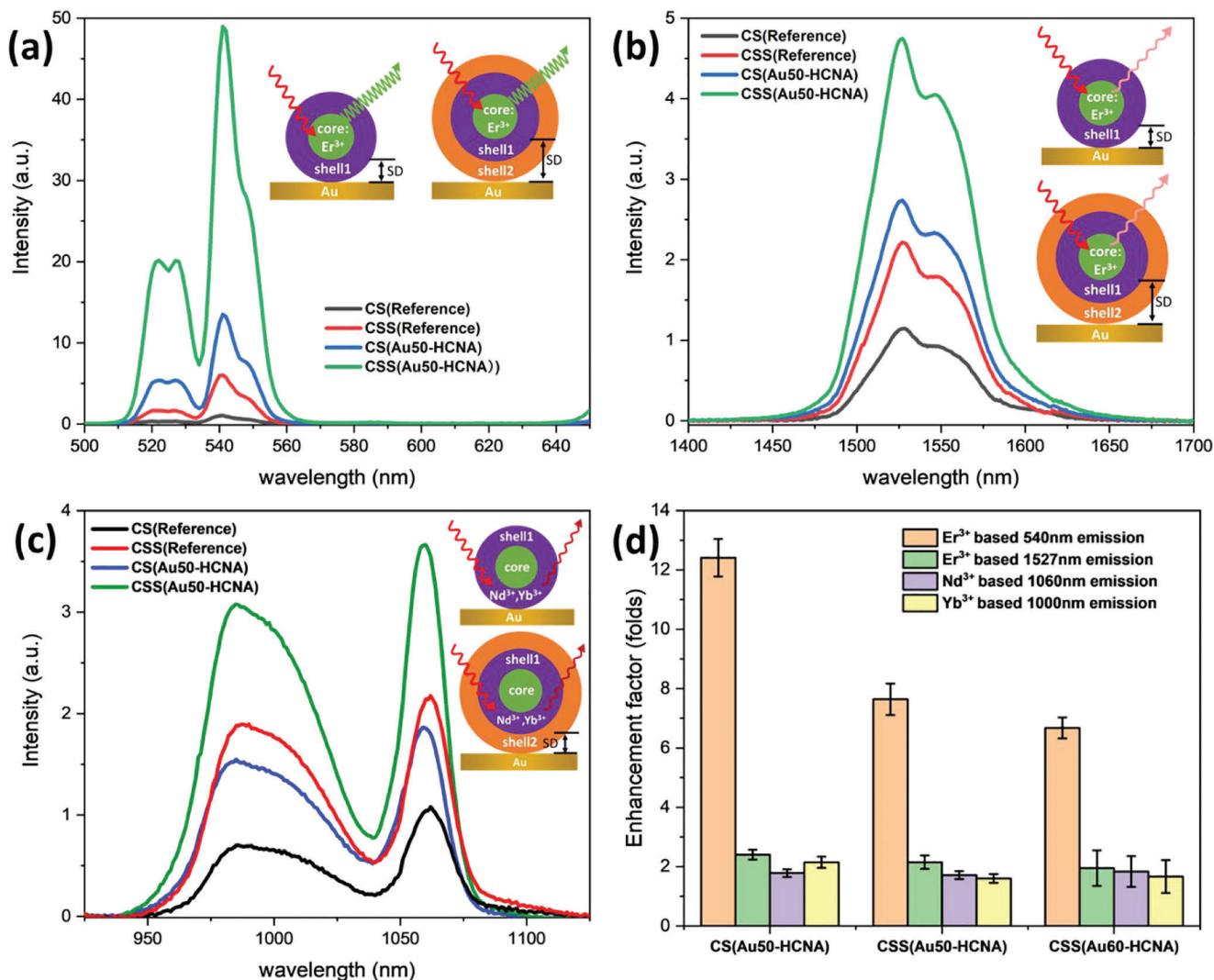


Figure 4. Photoluminescence spectra of a) Er³⁺ induced visible UCL, b) Er³⁺ induced NIR-II DCL c) Nd³⁺ and Yb³⁺ induced NIR-II DCL from CS and CSS DCNPs coated Au50-HCNA hybrid films, insets a–c): schematic illustrations show the separation distance (SD) between corresponding emitting ions and Au surface in CS and CSS configurations. Inset a): SD is ≈ 3.4 nm for CS (left) and ≈ 5.9 nm for CSS (right). Inset b): SD is ≈ 3.4 nm for CS (upper) and ≈ 5.9 nm for CSS (bottom). Inset c): SD is ≈ 2.5 nm for CSS (bottom). d) Plot of fluorescence enhancement factors for DCNPs on Au-HCNA.

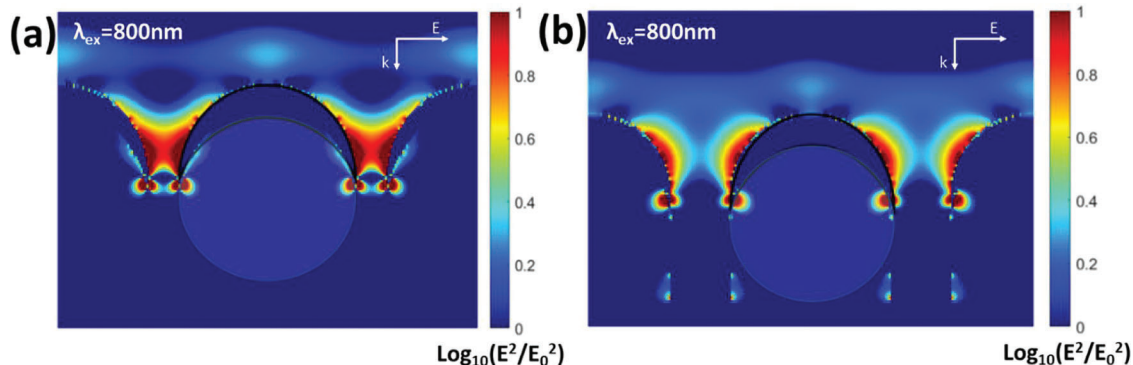


Figure 5. Local E-field enhancement calculated with 3D finite-difference time-domain (FDTD) modelling for a) Au50-HCNA and b) Au60-HCNA, using a linearly polarized 800 nm excitation beam source. The figure shows the cross-sectional E-field mapping through the center of Au-HCNA while k and E stand for wave-vector and electric-field polarization of excitation source, respectively. The unit bar of each e-field plot indicates the normalized value of E^2 in logarithmic scale where the log is to base 10.

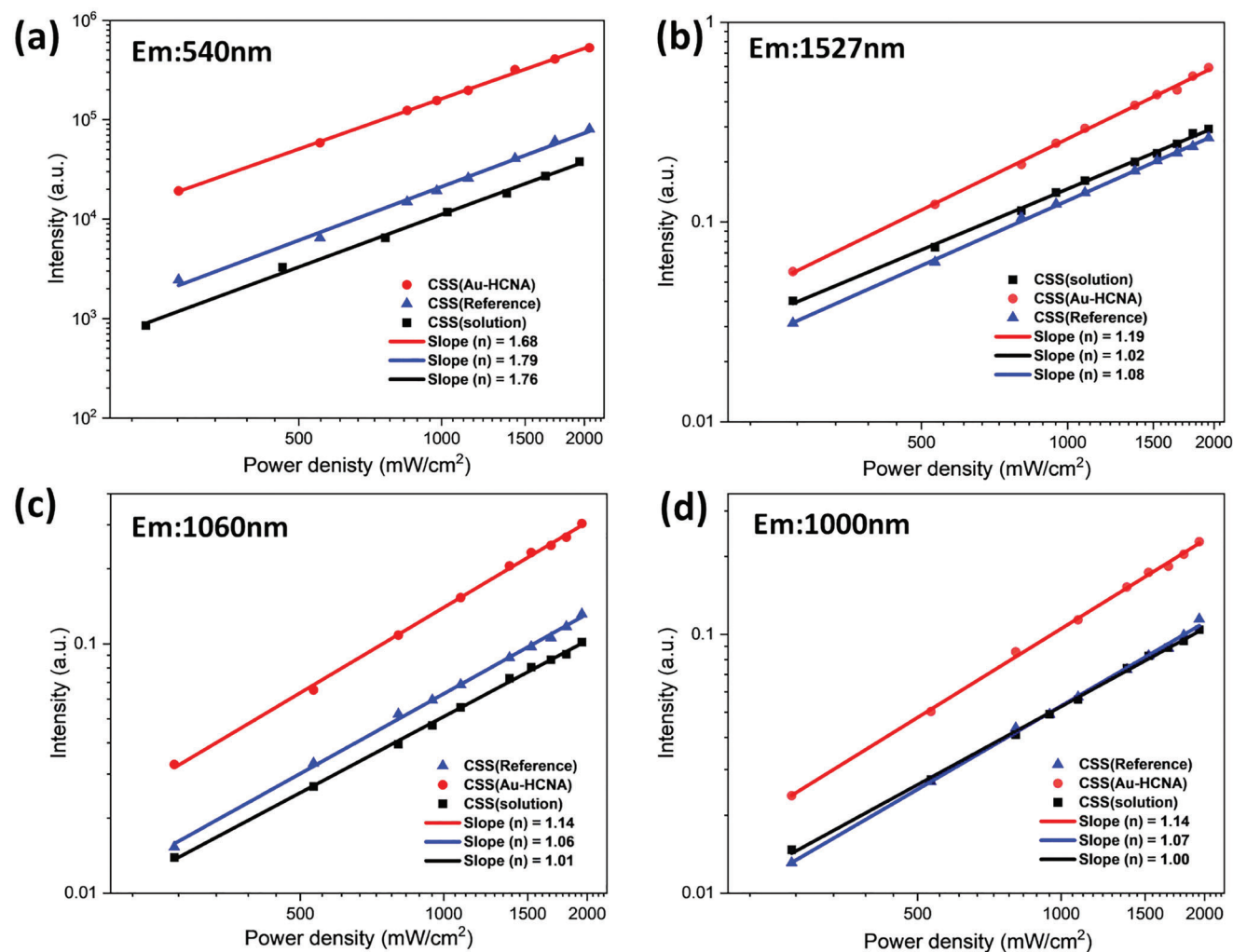


Figure 6. Log–log plots of excitation power dependent fluorescence at a) 540 nm, b) 1527 nm, c) 1060 nm, and d) 1000 nm, respectively, for the DCNPs in cyclohexane, on pristine FTO glass and Au50-HCNA.

was noted the maximum E-field intensity enhancement for both types of Au-HCNAs was located between adjacent Au caps.

The excitation rate of DCNPs distributed in areas of high electric field can be accelerated and show a proportional relation with E-field intensity enhancement^[25c]

$$r_0 \propto E_0^2 \quad (1)$$

$$\frac{r}{r_0} \propto \frac{E^2}{E_0^2} \quad (2)$$

where r_0 and r denote the original and the accelerated transition rate of sensitizer ions incorporated in DCNPs. E is the electric field amplitude and E_0 is the magnitude of the incident electric field, so that

“ E^2/E_0^2 ” is then the E-field intensity enhancement. Although the extinction peak of Au60-HCNA showed a higher degree of overlap with the excitation band at 808 nm compared to the extinction peak of Au50-HCNA, the E-field intensity enhancement

for Au50-HCNA was higher. One possible explanation could be a higher degree of SPR coupling from Au50-HCNA, owing to the smaller separation distance between adjacent Au caps. This may also explain the slightly higher UCL and DCL enhancement factors for CSS-DCNPs coupled with Au50-HCNA compared to those coupled with Au60-HCNA.

Figure 6 shows the log-log plots of excitation power dependent fluorescence of DCNPs in solution, on pristine FTO glass and on Au-HCNA. For Er³⁺ induced UCL emission, the fluorescence intensity showed a nearly quadratic dependence on the excitation power density in the weak power density regime (<5 W cm⁻²), while the power dependence of DCNPs on Au-HCNA and on the FTO glass reference, as well as in solution, showed negligible differences. This observation was consistent with our previous report^[46] and proved the UCL from lanthanide nanoparticles was dominated by a “two-photon” process, regardless of the medium and plasmonic modulations. All the NIR-II emissions from Er³⁺, Nd³⁺ and Yb³⁺ showed a nearly linear dependence on the excitation power density, which agreed with the reported “one photon” DCL process.^[26] In general, the emission intensity (I) and

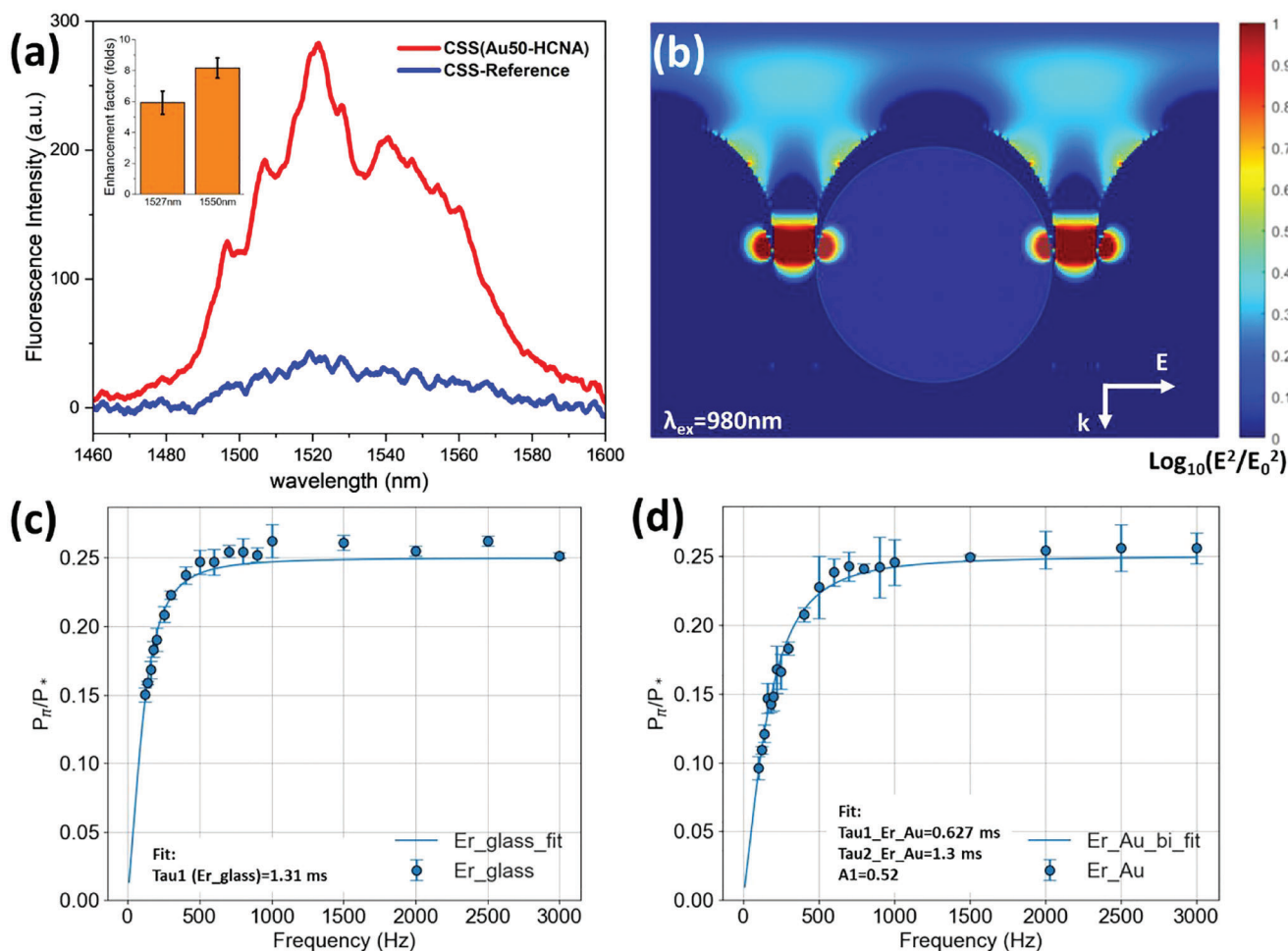


Figure 7. Plasmonic modulation on Er^{3+} induced NIR-II DCL enhancement under 980 nm excitation via studying a) photoluminescence spectra of CSS-DCNPs on glass and on Au50-HCNA, inset: Er^{3+} emitted NIR-II-fluorescence enhancement factor at the single wavelength. b) Local E-field enhancement calculated by 3D-FDTD modelling for Au-50 HCNA, using linear polarized 980 nm excitation beam source. c) Er^{3+} emitted 1550 nm lifetime of pristine CSS-DCNP on glass and the fitting curve by the monoexponential fit d) Er^{3+} emitted 1550 nm lifetime of CSS-DCNP coupled with Au50-HCNA and the corresponding bi-exponential (blue) fit curves.

E-field intensity (E^2) showed a relation of “ $I \propto E^{2n}$ ” for the n-photon process.^[25c] As a result, the emission efficiency of “two-photon” UCL had a fourth power dependence on the E-field enhancement (E/E_0), whilst the “one photon” DCL process of NIR-II DCL had a quadratic dependence.^[25a] This can be a rational explanation of the observation that the enhancement factor observed in NIR-II-DCL was lower than the enhancement factor observed in visible-UCL.

Figure 7a shows that Er^{3+} emitted NIR-II-DCL under 980 nm excitation can be enhanced up to 5.8- and 8.2-fold from CSS-DCNPs/Au50-HCNA hybrid film, at 1527 and 1550 nm respectively. Note that this observed fluorescence was an average of Er^{3+} that were coupled to SPR and those that were not. To further investigate the underlying physical mechanisms of plasmon induced NIR-II DCL enhancement, the plasmonic effects on the excitation process of Yb^{3+} at 980 nm, as well as the NIR-II emission process corresponding to $^4I_{13/2}(\text{Er}^{3+}) \rightarrow ^4I_{15/2}(\text{Er}^{3+})$ decay was studied using FDTD simulations and lifetime measurements. The simulated E-field intensity mapping at 980 nm (Figure 7b)

showed that the incident field was concentrated at the closest separation between adjacent Au caps, with the maximum enhancement (E^2/E_0^2) being ≈ 10 fold. Meanwhile, the E-field intensity enhancement on top of Au caps varied from 1 to ≈ 6 -fold depending on the relative positions across metal surface. If no other factors were considered, the excitation enhancement can contribute to a maximum ≈ 10 -fold improvement in NIR-II DCL emission of DCNPs in hot spots. However, complexity may arise from the increased radiative and nonradiative decay rate from the populated $^2F_{5/2}(\text{Yb}^{3+})$ states, leading to the faster depopulation of $^4I_{11/2}(\text{Er}^{3+})$ states and suppression of DCL processes.^[25c,27]

Figure 7c shows that the fluorescence decay curve at 1550 nm for CSS-DCNPs on FTO glass was well fitted by monoexponential function and the estimated lifetime was ≈ 1.3 ms. Figure 7d shows the fitting of the fluorescence decay curve for CSS-DCNPs/Au50-HCNA was done for two distinct emitter lifetimes, equivalent to a bi-exponential fit. Also note that $\approx 52\%$ of emitted photons originated from SPR coupled DCNPs as the lifetime of this portion was decreased to 0.627 ms. The other $\approx 48\%$

of emitted photons were derived from DCNPs which were unaffected by SPR, while the lifetime of this part was close to the intrinsic lifetime on FTO glass. Previous reports showed that both radiative and nonradiative rates of fluorophores near a plasmonic nanostructure could be modified, providing an overlap between the emission wavelength of fluorophores and surface plasmon resonance.^[22,24b,28] For the CSS structure, the nonradiative energy transfer or “FRET” process from the metallic surface was significantly prevented as emitting Er³⁺ was protected by an overall 6 nm shell, with a net fluorescence enhancement being observed from photoluminescence spectra. As a result, the ratio of SPR-coupled quantum yield to the intrinsic quantum yields of DCNPs, as well as the radiative emission enhancement factor can be estimated in the low excitation region, according to the Equations (3)–(7)^[29]

$$S_{Au} = N_{Er}(a\Gamma_{rad}E_0^2 + (1 - a)\Gamma'_{rad}E^2) \quad (3)$$

$$S_{glass} = N_{Er}\Gamma_{rad}E_0^2 \quad (4)$$

$$Enh_{total} = \frac{S_{Au}}{S_{glass}} = a + (1 - a)\frac{\Gamma'_{rad}E^2}{\Gamma_{rad}E_0^2} \quad (5)$$

$$\Gamma_{rad} = \eta\Gamma_{total} \quad (6)$$

$$\frac{\Gamma'_{total}}{\Gamma_{total}} = \frac{\Gamma'_{rad}/\eta'}{\Gamma_{rad}/\eta} = \frac{\Gamma'_{rad} \times \eta}{\Gamma_{rad} \times \eta'} \quad (7)$$

where S_{Au} and S_{glass} denote the emitted photons from CSS-DCNP/Au50-HCNA and CSS-DCNP/FTO glass substrates, respectively. N_{Er} is the total amount of Er³⁺ applied on each substrate. a is the fraction of DCNPs uncoupled with Au50-HCNA. Γ_{rad} and Γ'_{rad} represent the intrinsic and SPR-coupled radiative decay rate of DCNPs, respectively. E^2 and E_0^2 are the excitation electric field intensities of the plasmonic hot spots and free space, respectively, while E^2/E_0^2 is regarded as E-field intensity enhancement. η and η' are the original and the SPR-modified quantum yield of DCNPs. Enh_{total} is the observed fluorescence enhancement at 1550 nm. Γ_{total} and Γ'_{total} are the intrinsic and SPR-modified and total decay rate equivalent to reciprocal value of SPR-modified lifetime and intrinsic lifetime of DCNPs, respectively.

Based on Figure 7b and Figure S3b (Supporting Information), we estimate that the SPR-coupled DCNPs occupied $\approx 60\%$ of all DCNPs coated onto Au50-HCNA, while the other $\approx 40\%$ of DCNPs were unaffected by the SPR. For those SPR-coupled DCNPs, $\approx 30\%$ of nanoparticles were distributed in hot spots where the excitation E-field intensity enhancement can reach a maximum of 10-fold, and the other portion of nanoparticles experienced E-field enhancements to varying degrees. To simplify the model, two extreme situations were considered: one assumes all SPR-coupled DCNPs experienced the maximum E-field enhancement; the other assumes that 30% of SPR-coupled DCNPs experienced the maximum E-field enhancement while the others experienced negligible E-field enhancement. As such, a valid

estimation should be within the scope of the two extreme conditions. With the known Enh_{total} , Γ_{total} and Γ'_{total} , the ratio of quantum yield between SPR-coupled DCNPs and original DCNPs was $2.7 \leq \eta'/\eta \leq 5.2$. This result proves a net enhancement in quantum yield via plasmonic modulation, confirming the crucial contribution of radiative emission enhancement to the observed fluorescence enhancement.

Since the DCNPs were simply drop-cast onto an Au nanoarray, the observed NIR-II emission enhancement was an averaged value over multiple layers of nanoparticles located at various distances from the metallic surface. Hence the measured enhancement factors were far lower than could be achieved with a monolayer of DCNPs distribute uniformly over the Au nanoarray with an appropriate separation distance. For future study, coating a monolayer of DCNPs onto plasmonic nanoarray films to achieve a higher NIR-II-DCL enhancement for practical biosensing work is worth investigating.

3. Conclusion

In this work NIR-II DCL enhancement from DCNPs coupled with Au-HCNA was demonstrated, for the first time. The plasmonic Au-HCNA films were successfully fabricated via a facile colloidal lithography method, with optically tuneable spectral characteristics. When CSS-DCNPs were placed in the vicinity of the Au-HCNA and excited by an 808 nm laser, emission intensities from Yb³⁺ induced 1000 nm, Nd³⁺ induced 1060 nm, and Er³⁺ induced 1527 nm emission were enhanced up to ≈ 2 fold. More importantly, emission intensity of Er³⁺ induced DCL at 1527 and 1550 nm were enhanced up to 6-fold and 8-fold under 980 nm excitation. 3D-FDTD simulation and lifetime measurement at 980 nm showed that both local E-field enhancement and increased radiative decay contributed to the observed Er³⁺ induced NIR-II DCL enhancement. This work demonstrates a novel strategy to enhance weak NIR-II DCNPs luminescence efficiency, paving the way for their bioimaging and/or biosensing applications in NIR-II.

4. Experimental Section

Chemicals and Materials: Oleic acid (OA 90%), 1-octadecenoic (ODE 90%), sodium hydroxide (NaOH), ammonium fluoride (NH₄F 96%), methanol ($\geq 99.9\%$), cyclohexane (99.5%), yttrium (III) acetate hydrate (99.9%), Erbium (III) acetate hydrate (99.9%), ytterbium acetate hydrate (99.9%), cerium(III) acetate hydrate (99.9%), hydrochloric acid (37%), poly(ethylene glycol) 2-aminoethyl ether acetic acid, sodium dodecyl sulfate (SDS, 98.5%), were purchased from Sigma Aldrich. Monodisperse polystyrene solution (10% w/v, 488 nm) was purchased from Bangs Laboratories. All the chemicals were used as received without any purification.

Synthesis of Core NaGdF₄:Yb/Er/Ce Nanoparticles: The core nanoparticles were synthesized through a modified co-precipitation method.^[30] Briefly, 0.74 mmol of Gadolinium (III) acetate hydrate, 0.02 mmol of Erbium (III) acetate hydrate (99.9%), 0.2 mmol of ytterbium (III) acetate hydrate (99.9%), and 0.04 mmol of Cerium (III) acetate hydrate (99.9%) powders were added into a 100 mL three-neck round bottom flask containing 7 mL of OA and 15 mL of ODE. The mixture was then heated up to 145 °C and kept for 1 h under a vacuum. When the solution was cooled down, 10 mL of methanol containing 4 mmol ammonium fluoride and 2.5 mmol sodium hydroxide was slowly added. The mixture solution was

then kept at 110 °C for 30 min to remove excess water and methanol, followed by heating up to 295 °C and maintaining the temperature for 60 min under a gentle argon gas flow. The solution was cooled down to RT and then washed with ethanol several times. The obtained product was resuspended in cyclohexane.

Synthesis of NaGdF₄: Yb/Er/Ce@NaGdF₄ Nd/Yb Core/Shell Nanoparticle: 0.85 mmol of Gadolinium (III) acetate, 0.1 mmol of ytterbium acetate (III), and 0.05 mmol of neodymium acetate (III) powders were combined with 7 mL OA and 15 mL ODE to form lanthanide oleate solution at 145 °C for 1 h. When the solution was cooled down to 50 °C, the above-mentioned NaGdF₄ core nanoparticle solution was immediately injected, and then the mixture was stirred for 30 min. 10 mL of methanol containing 4 mmol ammonium fluoride and 2.5 mmol sodium hydroxide was then slowly added. The mixture solution was then kept at 110 °C for 30 min to remove excess water and methanol and cyclohexane, followed by heating up to 295 °C and maintaining the temperature for 90 min under a gentle argon gas flow. The solution was then cooled down to RT and washed in the same way as the NaGdF₄ core nanoparticle solution and was finally redispersed in cyclohexane.

Synthesis of NaGdF₄: Yb/Er/Ce@NaGdF₄ Nd/Yb@NaGdF₄ Core/Shell/Shell nanoparticles: 1 mmol of Gadolinium (III) acetate was dissolved in 7 mL OA and 15 mL ODE to form lanthanide oleate solution at 145 °C for 1 h. When the solution was cooled down to 50 °C, the above-mentioned stock core/shell nanoparticle solution was injected, followed by adding 10 mL of methanol containing 4 mmol ammonium fluoride and 2.5 mmol sodium hydroxide. The solution was heated to 110 °C, held at 110 °C for 30 min, and then was heated up to 295 °C under argon flow with vigorous stirring for 90 min. The solution was then cooled down, washed off by ethanol, and finally redispersed in cyclohexane.

Assembly of a Monolayer of PS Beads on the Substrate: A monolayer of hexagonal ordered PS beads was deposited onto the hydrophilic surface of a FTO glass substrate by using a self-assembly technique according to the previous reports.^[16c,31] Briefly, FTO glass slides and a silicon wafer were sequentially cleaned with acetone, ethanol, and DI water, each for 10 min. To enhance their hydrophilicity, all substrates were exposed to UV–ozone for 120 min after drying. Meanwhile, the commercialized PS beads (≈488 nm in diameter) solution was diluted by mixing with ethanol at a volumetric ratio of 1:1, followed by sonication for 10 min. An aliquot of diluted PS solution (≈3–5 μL) was deposited onto the silicon wafer dropwise. When the PS beads were completely spread out and dried, the wafer was slowly immersed into a 15 cm glass vessel filled with 200 mL of DI-water containing several drops of 2% SDS solution, resulting in the monolayer assembly to detach from the silicon wafer. The PS bead monolayer assembly was finally transferred from water onto FTO glasses and dried under a fume hood for 24 h.

Fabrication of Au Hole-Cap Nanoarrays (Au-HCNA): Au-HCNA films were fabricated and modified through a previously reported colloidal lithography method.^[32] The as-prepared PS beads assembly substrate was treated by Reactive Ion Etching (RIE) using O₂ for 50 s and 60 s, with an O₂ pressure of 20 Pa, RF power of 100 W, and O₂ flow of 20 sccm. Later, a 60 nm of Au layer was coated on the substrate surface via Magnetron sputtering using a Mantis deposition system. The height of the Au layer was monitored by a quartz crystal monitor (QCM) in the sputtering system. The final products treated by 50 s and 60 s of RIE were labelled as Au50-HCNA and Au60-HCNA.

Deposition of Multilayered DCNPs on Au-HCNA: The as-prepared DCNP solution was diluted to around 1 mg mL⁻¹, followed by depositing 9 μL of DCNP solution onto the center of gold hole-cap arrays via drop-casting. The sample was placed under the fume hood for at least 30 min until the solvent was completely evaporated. As a reference, the same amount of DCNPs was deposited onto the pristine FTO glass slides using the same drop-casting technique.

Characterization Techniques: X-ray diffraction (XRD) patterns of core, core–shell, core–shell–shell DCNPs, and each substrate sample were measured by PANalytical X-ray Diffractometer with Cu Kα irradiation ($K = 1.5406 \text{ \AA}$), in the 2θ range from 15° to 65°, at a scanning rate of 4° per minute. Both low and high-resolution transmission electron microscopy

(TEM) images of DCNPs were recorded on a JEOL-2010F TEM equipped with energy-dispersive X-ray spectroscopy (EDX, Oxford Instruments, UK), at an accelerating voltage of 200 kV. Scanning electron microscope (SEM) images of substrate samples were recorded on an LEO Gemini 1525 Field Emission Gun SEM (Carl Zeiss Microscope GmbH, UK), using an InLens detector at an acceleration voltage of 5 kV. The equipped Energy-dispersive X-ray spectroscopy (EDX, from Oxford Instruments, UK) mode was performed at 20 kV. The cross-sectional SEM image was made by a Helios NanoLab 600 at 2 kV. Topographies of the substrates were characterized by an MFP-3D classic Atomic Force Microscope (AFM, from Asylum Research). The scans were taken using the tapping mode.

The absorption spectra were measured on a Cary 5000 UV–Vis–NIR spectrophotometer, with a scan range of 400 nm–2000 nm for the substrate sample, and 700–1400 nm for the solution sample. Fluorescence spectra of DCNPs in solution and on the substrates were characterized by the Fluorolog Tau3 system (Horiba Scientific) equipped with the MDL-808 nm (continuous wave, tuneable power supply) laser (from Changchun New Industries Optoelectronics Technology Co., Ltd.). The visible UCL emission spectra (500–900 nm) were collected by using a self-contained Photon Counting PMT Detection System. The NIR-II/III DCL spectra (950–1800 nm) were collected by using a 512 element TE-cooled InGaAs array near-IR detector. The angle of acquisition was fixed at 30° for the consistency and accuracy of each measurement.

Numerical Modeling: Electromagnetic analysis of the Au hole-cap nanoarrays (Au-HCNA) was carried out using the open-source Finite Difference Time Domain (FDTD) software MEEP.^[33] It should be noted that electromagnetic analysis can be carried out using other computational electromagnetic techniques, such as finite element or multiple multipole methods.^[34] FDTD was chosen because it is relatively straightforward to implement when the geometry is comparatively complex and where results are needed over a wide spectral range. It has previously been used by the group to predict electric field enhancement and MEF emission enhancement due to Au and Ag nanoparticles (see for example^[16c,35]).

The model consisted of a PS sphere hexagonal array on an FTO glass substrate. The sphere diameter for Au50-HCNA and Au60-HCNA was 467 nm and 399 nm respectively, and a Au layer of 60 nm covered the top surfaces of the FTO and PS. A graphical representation of this geometry can be observed in Scheme 1d. In the FDTD model the Au was modelled using a Drude–Lorentz model whilst the PS nanosphere and the FTO had refractive index of 1.54 and 1.47, respectively. The upper and lower boundaries of the computational domain are terminated using perfectly matched layers (PMLs) to prevent any nonphysical reflections, and periodic boundaries were used in the other two dimensions to model an infinite hexagonal array of PS nanospheres with nanocap arrays. The FDTD cell resolution was 5 nm in each direction, which was found by convergence testing. The simulations were run using the ARCHIE-WEST High-Performance Computer (www.archie-west.ac.uk). The reflections from the array, transmission into the FTO and the Au absorption, were calculated using a method described previously,^[36] where the incident, transmitted and backscattered fields are found through computational surfaces placed in the FTO and above the array. The array was excited using an incident plane wave normal to the upper surface.

Lifetime Measurements: The lifetime of pristine CSS-DCNP on glass and CSS-DCNP coupled with Au50-HCNA were measured using a frequency domain lifetime measurement technique with modulated pump and detection technique.^[29] Au50-HCNA was chosen due to the fact that excitation of Au50-HCNA at 980 nm is expected to well resonate with the sensitization of Yb³⁺, while E-field enhancement may play a role in the Er³⁺ induced NIR-II DCL. The lifetime study will shed the light on the radiative decay enhancement of DCNPs coupled to Au-HCNA, with the aim of estimating the contribution of E-field and radiative decay enhancement to the overall Er³⁺ induced NIR-II DCL enhancement. Both the pump light and the fluorescence were focused through mechanical choppers to produce near-square-wave response. The excited state lifetime of erbium ions for square wave excitation at a frequency ν over a single period of modulation, $T = \nu^{-1}$, can be described by a three-level model. Assuming rapid transition of electrons from the excited $^4I_{11/2}$ state to the $^4I_{13/2}$ fluorescent state, and a low pump rate to avoid state saturation, a single differential

equation describes the population of the $^4I_{13/2}$ fluorescent state

$$\frac{dN}{dt} = -\frac{N}{\tau} + R(t)N_T \quad (8)$$

where $R = r$ for $0 < t < T/2$ and $R = 0$ for $T/2 < t < T$. The emitted signal under continuous excitation is $S_0 = N/\tau = rN_T$. The resulting signal, $S(t) = N(t)/\tau$ is

$$S(t) = S_0 \left(1 - \frac{e^{-t/\tau}}{1 + e^{-T/2\tau}} \right), 0 < t < \frac{T}{2} \quad (9)$$

$$S(t) = S_0 \frac{e^{-(t-T/2)/\tau}}{1 + e^{-T/2\tau}}, \frac{T}{2} < t < T \quad (10)$$

For a modulation frequency, ν , and integration time, t_{int} , the spectrometer integrates over νt_{int} periods. Assuming an experimental collection and detection efficiency of η , when the two choppers are out of phase ($\phi = \pi$), the spectrometer measures a signal

$$P_\pi(\nu) = \eta \nu t_{int} S_0 \int_{T/2}^T S(t) dt = \nu P_* \tanh((4\nu\tau)^{-1}) \quad (11)$$

To normalize this signal, the sample fluorescence without the two choppers over the same integration time was measured, to find $P_* = \eta t_{int} S_0$. The ratio of the two measurements, $F(\nu)$, yields the lifetime

$$F(\nu) = \frac{P_\pi(\nu)}{P_*} = \nu\tau \tanh((4\nu\tau)^{-1}) \quad (12)$$

For a collection of emitters with a mono-exponential decay, the lifetime is returned for each measurement of $F(\nu)$. In the case of mixtures of emitters with differing lifetimes, an average signal will be found

$$P_\pi(\nu) = P_* \sum_i^N a_i \nu \tau_i \tanh((4\nu\tau_i)^{-1}) \quad (13)$$

where a_i are the proportions of emitted photons from the emitters with lifetimes, τ_i , and $\sum_i a_i = 1$. In the case of a bi-exponential decay, which incorporates both DCNPs close and away from the hotspot regime resulting in two different emission rates, the fitting is done as a two-emitter lifetime system. The fluorescence lifetime data has been fitted by using the python package `scipy.optimize.curve_fit` V0.19 developed by Scipy, which uses a nonlinear least squares to fit a function to the data. The fitting function was chosen based on the physics model examined, and the quality of the fit where the fitting error is formulated as: $\chi^2 = \sum_{i=1}^n \left(\frac{y_i - f(x_i)}{\sigma_{y_i}} \right)^2$, where y_i is the value of the raw data, σ_{y_i} is the uncertainty of y_i , and $f(x_i)$ is the fitting result of each y_i .

Supporting Information

Supporting Information is available from the Wiley Online Library or from the author.

Acknowledgements

This work was supported by Imperial College London, the President's Excellence Fund for Frontier Research (awarded in 2021). The authors acknowledge the use of characterization facilities within the Harvey Flower Electron Microscopy Suite at the Department of Materials, Imperial College London. The authors acknowledge support from the Henry Royce Institute made through EPSRC grant EP/R00661X/1.

Conflict of Interest

The authors declare no conflict of interest.

Data Availability Statement

The data that support the findings of this study are available from the corresponding author upon reasonable request.

Keywords

NIR-II downconversion, plasmonic, nanoparticles, fluorescence enhancement

Received: February 24, 2023

Revised: May 17, 2023

Published online: June 20, 2023

- [1] a) Kenry, Y. Duan, B. Liu, *Adv. Mater.* **2018**, *30*, 1802394; b) S. Diao, J. L. Blackburn, G. Hong, A. L. Antaris, J. Chang, J. Z. Wu, B. Zhang, K. Cheng, C. J. Kuo, H. Dai, *Angew. Chem., Int. Ed.* **2015**, *54*, 14758.
- [2] K. Welsher, S. P. Sherlock, H. Dai, *Proc. Natl. Acad. Sci. USA* **2011**, *108*, 8943.
- [3] L. Li, X. Dong, J. Li, J. Wei, *Dyes Pigm.* **2020**, *183*, 108756.
- [4] H. M. Gil, T. W. Price, K. Chelani, J. G. Bouillard, S. D. Calaminus, G. J. Stasiuk, *iScience* **2021**, *24*, 102189.
- [5] a) R. Wang, F. Zhang, *J. Mater. Chem. B* **2014**, *2*, 2422; b) X. Dang, L. Gu, J. Qi, S. Correa, G. Zhang, A. M. Belcher, P. T. Hammond, *Proc. Natl. Acad. Sci. USA* **2016**, *113*, 5179; c) X. Jiang, R. Pu, C. Wang, J. Xu, Y. Tang, S. Qi, Q. Zhan, X. Wei, B. Gu, *Biomed. Opt. Express* **2021**, *12*, 6984; d) N. N. Zhang, C. Y. Lu, M. J. Chen, X. L. Xu, G. F. Shu, Y. Z. Du, J. S. Ji, *J. Nanobiotechnol.* **2021**, *19*, 132.
- [6] M. Yamanaka, H. Nioka, T. Furukawa, N. Nishizawa, *J. Biomed. Opt.* **2019**, *24*, 070501.
- [7] Y. Zhang, Y. Shi, Z. Qin, M. Song, W. Qin, *Nanomaterials* **2018**, *8*, 615.
- [8] C. Cheng, Y. Xu, G. De, J. Wang, W. Wu, Y. Tian, S. Wang, *CrystEngComm* **2020**, *22*, 6330.
- [9] a) Y. Yang, D. Tu, Y. Zhang, P. Zhang, X. Chen, *iScience* **2021**, *24*, 102062; b) H. Li, X. Wang, T. Y. Ohulchanskyy, G. Chen, *Adv. Mater.* **2021**, *33*, 2000678.
- [10] a) J. C. G. Bünzli, S. V. Eliseeva, *Chem. Sci.* **2013**, *4*, 1939; b) Y. Fan, F. Zhang, *Adv. Opt. Mater.* **2019**, *7*, 1801417.
- [11] a) A. Schroter, S. Märkl, N. Weitzel, T. Hirsch, *Adv. Funct. Mater.* **2022**, *32*, 2113065; b) N. J. Johnson, S. He, S. Diao, E. M. Chan, H. Dai, A. Almutairi, *J. Am. Chem. Soc.* **2017**, *139*, 3275; c) Z. Luo, D. Hu, D. Gao, Z. Yi, H. Zheng, Z. Sheng, X. Liu, *Adv. Mater.* **2021**, *33*, 2102950; d) B. Xu, D. Li, Z. Huang, C. Tang, W. Mo, Y. Ma, *Dalton Trans.* **2018**, *47*, 7534.
- [12] B. Chen, F. Wang, *Acc. Chem. Res.* **2020**, *53*, 358.
- [13] Y. Zhong, Z. Ma, S. Zhu, J. Yue, M. Zhang, A. L. Antaris, J. Yuan, R. Cui, H. Wan, Y. Zhou, W. Wang, N. F. Huang, J. Luo, Z. Hu, H. Dai, *Nat. Commun.* **2017**, *8*, 737.
- [14] Y. Li, M. Jiang, Z. Xue, S. Zeng, *Theranostics* **2020**, *10*, 6875.
- [15] Y. Li, C. Liu, P. Zhang, J. Huang, H. Ning, P. Xiao, Y. Hou, L. Jing, M. Gao, *Front Chem.* **2020**, *8*, 832.
- [16] a) E. M. Goldys, A. Barnett, F. Xie, K. Drozdowicz-Tomsia, I. Gryczynski, E. G. Matveeva, Z. Gryczynski, T. Shtoyko, *Appl. Phys. A: Mater. Sci. Process.* **2007**, *89*, 265; b) C. Joyce, S. M. Fothergill, F. Xie, *Mater. Today Adv.* **2020**, *7*, 100073; c) J. S. Pang, I. G. Theodorou, A. Centeno, P. K. Petrov, N. M. Alford, M. P. Ryan, F. Xie, *ACS Appl. Mater. Interfaces* **2019**, *11*, 23083.

- [17] a) W. Park, D. Lu, S. Ahn, *Chem. Soc. Rev.* **2015**, *44*, 2940; b) I. L. Rasskazov, L. Wang, C. J. Murphy, R. Bhargava, P. S. Carney, *Opt. Mater. Express* **2018**, *8*, 3787; c) W. Bi, Y. Wu, C. Chen, D. Zhou, Z. Song, D. Li, G. Chen, Q. Dai, Y. Zhu, H. Song, *ACS Appl. Mater. Interfaces* **2020**, *12*, 24737; d) J. Park, K. Kim, E. J. Jo, W. Kim, H. Kim, R. Lee, J. Y. Lee, J. Y. Jo, M. Kim, G. Y. Jung, *Nanoscale* **2019**, *11*, 22813.
- [18] a) A. Chu, H. He, Z. Yin, R. Peng, H. Yang, X. Gao, D. Luo, R. Chen, G. Xing, Y. J. Liu, *ACS Appl. Mater. Interfaces* **2019**, *12*, 1292; b) D. Lu, S. K. Cho, S. Ahn, L. Brun, C. J. Summers, W. Park, *ACS Nano* **2014**, *8*, 7780.
- [19] M. Saboktakin, X. Ye, U. K. Chettiar, N. Engheta, C. B. Murray, C. R. Kagan, *ACS Nano* **2013**, *7*, 7186.
- [20] Z. Yin, D. Zhou, W. Xu, S. Cui, X. Chen, H. Wang, S. Xu, H. Song, *ACS Appl. Mater. Interfaces* **2016**, *8*, 11667.
- [21] a) R. Bardhan, N. K. Grady, J. R. Cole, A. Joshi, N. J. Halas, *ACS Nano* **2009**, *3*, 744; b) T. Soller, M. Ringler, M. Wunderlich, T. A. Klar, J. Feldmann, H. P. Josel, Y. Markert, A. Nichtl, K. Kürzinger, *Nano Lett.* **2007**, *7*, 1941.
- [22] H. Qin, A. E. Shams, A. Centeno, I. G. Theodorou, A. P. Mihai, M. P. Ryan, F. Xie, *Phys. Chem. Chem. Phys.* **2017**, *19*, 19159.
- [23] A. L. Feng, M. L. You, L. Tian, S. Singamaneni, M. Liu, Z. Duan, T. J. Lu, F. Xu, M. Lin, *Sci. Rep.* **2015**, *5*, 7779.
- [24] a) J. R. Lakowicz, *Anal. Biochem.* **2005**, *337*, 171; b) J. Xu, W. Morton, D. Jones, T. A. Tabish, M. P. Ryan, F. Xie, *Appl. Phys. Rev.* **2022**, *9*, 031406.
- [25] a) J. Dong, W. Gao, Q. Han, Y. Wang, J. Qi, X. Yan, M. Sun, *Rev. Phys.* **2019**, *4*, 100026; b) S. Han, R. Deng, X. Xie, X. Liu, *Angew. Chem., Int. Ed.* **2014**, *53*, 11702; c) D. M. Wu, A. García-Etxarri, A. Salleo, J. A. Dionne, *J. Phys. Chem. Lett.* **2014**, *5*, 4020.
- [26] X. Lei, R. Li, D. Tu, X. Shang, Y. Liu, W. You, C. Sun, F. Zhang, X. Chen, *Chem. Sci.* **2018**, *9*, 4682.
- [27] F. Kang, J. He, T. Sun, Z. Y. Bao, F. Wang, D. Y. Lei, *Adv. Funct. Mater.* **2017**, *27*, 1701842.
- [28] I. G. Theodorou, Z. A. Jawad, Q. Jiang, E. O. Aboagye, A. E. Porter, M. P. Ryan, F. Xie, *Chem. Mater.* **2017**, *29*, 6916.
- [29] N. A. Günsken, M. Fu, M. Zapf, M. P. Nielsen, P. Dichtl, R. Röder, A. S. Clark, S. A. Maier, C. Ronning, R. F. Oulton, *Arch. Phys.* **2022**, *2202*, 08927.
- [30] F. Wang, R. Deng, X. Liu, *Nat. Protoc.* **2014**, *9*, 1634.
- [31] F. Xie, A. Centeno, M. R. Ryan, D. J. Riley, N. M. Alford, *J. Mater. Chem. B* **2012**, *1*, 536.
- [32] T. M. Schmidt, M. Frederiksen, V. Bochenkov, D. S. Sutherland, *Beilstein J. Nanotechnol.* **2015**, *6*, 1.
- [33] A. F. Oskooi, D. Roundy, M. Ibanescu, P. Bermel, J. D. Joannopoulos, S. G. Johnson, *Comput. Phys. Commun.* **2010**, *181*, 687.
- [34] C. G. Khoury, S. J. Norton, T. Vodinh, *ACS Nano* **2009**, *3*, 2776.
- [35] F. Xie, J. S. Pang, A. Centeno, M. P. Ryan, D. J. Riley, N. M. Alford, *Nano Res.* **2013**, *6*, 496.
- [36] A. Centeno, *APACE IEEE* **2003**, *2003*, 128.